SI Appendix for

Fluid-driven Origami-inspired Artificial Muscles

Shuguang Li,[1,2] Daniel M. Vogt,[1] Daniela Rus,[2] Robert J. Wood[1]

[1]John A. Paulson School of Engineering and Applied Sciences,
and the Wyss Institute for Biologically Inspired Engineering, Harvard University,
Cambridge, MA 02138, USA
[2]Computer Science and Artificial Intelligence Laboratory, Massachusetts Institute of Technology,
Cambridge, MA 02139, USA

Contents

1 Modeling and validation

We developed a simplified mechanical model to predict the force production of the artificial muscle. In this model, a linear zigzag actuator can be abstracted as a chain of triangular-cylinder-shaped units. Each of these units can be modeled as two hinged rigid beams with an initial opening angle 2θ, and the hinge can be modeled as two cantilever springs (Fig. S1(a)). For the artificial muscles with parallel skeleton walls, each structural void can be modeled as two parallel plates connected by a compression spring (Fig. S1(b)). This modeling method can be used to describe our artificial muscles with other skeleton structures. In addition, the skin of each artificial muscle unit is modeled as a mass-less, flexible, and non-stretchable membrane between two beams, forming a void. This membrane's geometry can be approximated as a parabolic arc and the skin's elongation and bending deformation are both neglected in our model.

For the blocked force estimation on a zigzag actuator, we used a force balancing method to describe the static forces at equilibrium. As written in Eq.**1**, the output force F_{output} equals to the sum of the horizontal tension forces T_x from the skin and the pushing force F_p applied on the cross-section area of the actuator, when there is a pressure difference ΔP between the inside and outside fluids of the muscle.

$$F_{output} = 2T_x + F_p \tag{1}$$

The force F_p in this model can be calculated as

$$F_p = \Delta P \times A = \Delta P H W \tag{2}$$

where A is the actuator's cross-section area, and W and H represent the width and height of the actuator, respectively. The force T_x is the horizontal part of the skin's tension force T, and

it can be calculated as

$$T_x = T\cos\beta \tag{3}$$

The tension force T can be estimated based on the Laplace Law as

$$T = \Delta P \times R \times W \tag{4}$$

and its angle to the horizontal direction is

$$\beta = \cos^{-1}(\frac{L}{R}) \tag{5}$$

where R is the radius of curvature of the skin at the contact point O. Using a parabolic curve to approximate the skin's curve, R can be estimated as

$$R = \frac{(1+(\frac{4h}{c})^2)^{\frac{3}{2}}}{\frac{8h}{c^2}} = \frac{L^2(1+(\frac{2h}{L})^2)^{\frac{3}{2}}}{2h} \tag{6}$$

In this equation, c is the chord length of the parabolic curve at the void's top ($c = 2L$), and h is the distance from the parabola's vertex to the void's top frame. Based on the experimental measurement of h and a given vacuum pressure ΔP, the output blocked force can be estimated.

To estimate the force-contraction relation, we built a model based on the principle of virtual work. The output force is a function of the hinge's angle at a constant pressure difference ΔP, it can be written as

$$F(\theta) \times 2\delta L(\theta) = -\Delta P \times \delta V(\theta) \tag{7}$$

$$F(\theta) = -\frac{\Delta P}{2}(\frac{\delta V(\theta)/\delta\theta}{\delta L(\theta)/\delta\theta}) \tag{8}$$

where δL and δV represent the small virtual changes of the unit void's opening length and the internal fluid's volume, respectively. L is a function of θ, and it can be written as

$$L(\theta) = D\sin\theta \tag{9}$$

$$\frac{\delta L(\theta)}{\delta\theta} = D\cos\theta \tag{10}$$

where D is the wall's length. The internal fluid's volume V can be approximated by subtracting a small triangular volume $V_{triangle}$ from the void's volume V_{void}.

$$V(\theta) = V_{void} - V_{triangle} \tag{11}$$

$$V_{void} = W \times A_{void} = WLH = WD^2 \sin\theta \cos\theta \tag{12}$$

$$V_{triangle} = W \times A_{triangle} = WLh = WD \sin\theta ({L_0}^2 - (D\sin\theta)^2)^{\frac{1}{2}} \tag{13}$$

where h is the subtracted triangular portion's height, and L_0 is half the void's opening length. We assume that the skin's total length in one void stays constant during the contraction, then h can be calculated as

$$h = \sqrt{({L_0}^2 - L^2)} = ({S_0}^2 - (D\sin\theta)^2)^{\frac{1}{2}} \tag{14}$$

$$L_0 = D\sin\theta_0 \tag{15}$$

where S_0 represents one half of the arc length from the original parabola approximation. This can be estimated by

$$S_0 = \frac{1}{2}(({L_0}^2 + 4{h_0}^2)^{\frac{1}{2}} + \frac{{L_0}^2}{2h_0}\sinh^{-1}(\frac{2h_0}{L_0})) \tag{16}$$

where h_0 is the measured depth of the parabolic approximation curve for the skin's initial deformation before contraction. We should note that the skin's length of each void can be estimated based on the void's geometry. However, the estimation accuracy highly depends on the stiffness of the skin material, and the sealing compactness between the skin and the skeleton. The fluid volume can then be written as:

$$V(\theta) = WD(D\sin\theta\cos\theta - \sin\theta({S_0}^2 - D^2\sin^2\theta)^{\frac{1}{2}}) \tag{17}$$

Let $\mu = {S_0}^2 - D^2\sin^2\theta$, we can get

$$\frac{\delta V}{\delta\theta} = WD(D(\cos^2\theta - \sin^2\theta) - \mu^{\frac{1}{2}}\cos\theta + \mu^{-\frac{1}{2}}D^2\sin^2\theta\cos\theta) \tag{18}$$

Based on Eqs. **10** and **18**, we can obtain a complete expression for Eq.**8**:

$$F(\theta) = -\frac{\Delta PW}{2}(\frac{D(\cos^2\theta - \sin^2\theta) - \mu^{\frac{1}{2}}\cos\theta + \mu^{-\frac{1}{2}}D^2\sin^2\theta\cos\theta}{\cos\theta}) \tag{19}$$

This force function should equal to zero when the voids are completely closed ($\theta = 0$) in practice. However, due to the inaccurate approximation of the fluid volume, this force estimation does not approach to zero.

$$F(0) = -\frac{\Delta PW}{2}(D - S_0) \tag{20}$$

To correct this force estimation, we introduced a linear correction term, $\lambda(\theta)$, into the model as shown in Eq. **21**. The force function can then be rewritten in Eq. **22** with the correction item.

$$\lambda(\theta) = 1 + \frac{(\theta_0 - \theta)(\frac{D}{S_0} - 1)}{\theta_0} \tag{21}$$

$$F(\theta) = -\frac{\Delta PW}{2}(\frac{D(\cos^2\theta - \sin^2\theta) - \lambda(\theta)(\mu^{\frac{1}{2}}\cos\theta - \mu^{-\frac{1}{2}}D^2\sin^2\theta\cos\theta)}{\cos\theta}) \tag{22}$$

The skeleton's elastic force can be estimated using a linear cantilever-spring model as

$$F_e(\theta) = k_s\Delta L = k_s(L_0 - D\sin\theta) \tag{23}$$

where k_s is the bending stiffness of the void's walls. Given the skeleton material's tensile modulus, k_s can be calculated by Eq. **24**.

$$k_s = \frac{EWt^3}{4D^3} \tag{24}$$

The net output force F_{output} can be estimated using equation (25), and the total contraction of a linear zigzag actuator with N units can be calculated using Eq. **26**:

$$F_{output}(\theta) = 2(F(\theta) - F_e(\theta)) \tag{25}$$

$$C(\theta) = N \times 2(L_0 - L(\theta)) = 2ND(\sin\theta_0 - \sin\theta) \tag{26}$$

To validate the model prediction, we performed experiments using three linear actuators with zigzag skeletons (Fig. S1(e)). We used a laser-based measurement to estimate the skin deformation (Fig. S1(f) and (g)). As shown in the comparison in Fig. S1(h) and 1(i), our model successfully predicts the blocked force and the force-contraction relationships for the linear zigzag actuators with three different configurations using 30-degree, 60-degree, and 90-degree folds. The prediction errors were approximately 7% for the blocked force, and 11% for the maximum free contraction at -70 kPa, respectively. The accuracy of our simplified model is acceptable for such a fluid-solid system made of both rigid and flexible materials, especially when the system is pneumatically driven at low pressure.

It should be noted that the linear zigzag structure used in this study is not optimally designed to maximize contraction or force, however the theoretical analysis and the prototype fabrication process are very convenient due to the simplicity of its geometry. Based on the mechanical model presented here, the linear zigzag muscle's geometry (e.g., the nominal fold angle) can be further optimized in order to produce the desired contractions and forces.

We should also note that we do not focus on deriving models and optimizing parameters for each particular muscle in this paper. However, the virtual-work based method is very generic, and it can be used to derive the force-contraction functions for a host of variations on the artificial muscles presented in this paper. Once their models are derived, many optimization methods and tools can be used to obtain the best designs for a desired performance (*1*).

2 Summary of performance characterization

We characterized the performance of a group of linear actuators using simple zigzag skeletons. As shown in Fig. S4(j) and (k), a nylon-fabric skin actuator (skin thickness: 0.34 mm, skeleton dimension: $120\times$ 60.5 $\times$14.5 mm^3) produced a free contraction of approximately 65 mm at -70 kPa – a contraction ratio of approximately 50%. A repeatable static contractile force of

approximately 200 N (at -70 kPa) was also obtained from this actuator. In addition, it is shown that the hysteresis on this actuator is relatively small (5 kPa). We then performed a 30,000-cycle load lifting test on this actuator. After this continuous 50-hour test, there was no observable performance reduction in either the blocked force or the contraction compared to the performance results obtained before this test (Fig. S4(j) and (k)).

We obtained a maximum blocked force from another nylon-fabric skin actuator (# 3 in Fig. S2(i) of approximately 428 N at -90 kPa. This force corresponds to an actuation stress of approximately 600 kPa that is roughly six times greater than the sustainable stress of mammalian skeletal muscle (100 kPa) (*2*).

The energy conversion efficiency and the power density of the artificial muscles were both measured on a miniature zigzag actuator made from polyester sheets. This light-weight actuator – similar in mass to a Ping-Pong ball – can be easily blown away by a small computer fan (Movie S7). In the power density measurement, the 2.6 g actuator can lift a 3 kg object (more than 1,000 times heavier than the actuator itself) within 0.2 seconds using a -80 kPa vacuum. A peak power density of 2.08 kW/kg was obtained during the 2 kg load lifting tests, and the peak power density calculated from the 1 kg load tests and the 3 kg load tests are 1.85 kW/kg and 1.80 kW/kg, respectively. All of these peak power densities are more than six times the peak power density of mammalian skeletal muscles (0.28 kW/kg) (*2*).

To measure the 2.6 g muscle's mechanical energy conversion efficiency, we conducted load-lifting experiments with different weights. As shown in Fig. S6(d), the averaged energy efficiency from the tests approached 23% (1 kg load, pneumatically driven) and 59% (0.5 kg load, hydraulically driven). The mechanical energy conversion efficiency for natural muscle is approximately (40%) (*2–4*).

To characterize the muscle system's energy conversion efficiency, we built an artificial muscle system using the light-weight zigzag muscle (weight: 2.6 g, length: 10 cm) directly powered

by an electric vacuum pump. Four different pumps were characterized in our experiment as shown in Fig. S6. In a previous experiment, we obtained a mechanical-to-mechanical energy efficiency approximately 20% from the pneumatic-driven muscle, however the electrical-to-mechanical energy efficiencies were approximately 2% - 5% (Fig. S6(c)), once these miniature diaphragm vacuum pumps were included into the system. Furthermore, the system's energy efficiency decreased to 0.3% when the muscle was powered by the large rotary vane pump. The miniature diaphragm pumps appear more efficient then the large rotary vane pump under these conditions. However, the large pump powered the muscle to lift the load up approximately 70 mm within 0.3 second in our experiment, and it was significantly more powerful than the miniature DC pumps. Therefore, various devices and energy sources should be considered for pressure generation in different practical applications. Our past work has quantified the relative merits (such as energy efficiency, energy density, and flow capacity) of various pneumatic energy sources, and the details can be found in (*5*).

The averaged system bandwidth of this 2.6 g linear muslce (with 500 g load) was approximately 1.1 Hz (-3 dB cutoff frequency). We should note that these experiments were conducted without any feedback control, and the system's bandwidth was also limited by the solenoid valve we used. Therefore, the bandwidth can be improved by using better valves and pressure regulators as well as a closed-loop controller (*6*). In addition, there are several powerful methods that can be implemented to potentially increase the bandwidth by 400% (*7*), for example increasing the flow rate and using filler materials inside of the muscles.

3 Actuator fabrication

We used different methods and materials to fabricate the actuators described in this paper (see Fig. S2(i) and Table S 1). The skeletons for the bending actuator, the three-finger hand, and all the actuators for static characterization are made of nylon materials using a desktop 3D printer

(The Mark One, Markforged, Inc.). The Onyx-based skeletons(Fig. S5(f)) were also fabricated by this printer. Another 3D printer (LulzBot TAZ 5, Aleph Objects, Inc.) was used to print the polyvinyl alcohol (PVA)-based skeleton for the water-soluble actuator (Fig.2(C) and Fig. S7(c)), and the TPU based skeletons for the large robotic arm(Fig. S7(f)). A laser cutter (Universal Laser Systems, Inc.) was also used for fabricating the skeletons. The skeletons for the miniature bio-compatible actuators were manually folded using crease patterns that were laser cut from a PEEK sheet (0.254 mm). Similarly, all the skeletons for the contraction, twisting, and gripping demos, as well as the 2.6 g light-weight actuator, were laser cut and manually folded using polyester sheets (a 0.127 mm sheet for the gripper, and a 0.254 mm sheet for the others). The skeletons for the large-scale lifter and the electronics-embedded actuator were both hinged from several laser-cut nylon and acrylic blocks (thickness: 3.175 mm), respectively. A stainless steel (316) shim (thickness: 0.254 mm) was manually formed to a zigzag-shaped skeleton for the underwater actuator. The skeleton of the cylindrical lifter is based on a compression spring made of 302 stainless steel (outside diameter: 22.5 mm, wire diameter: 1.25 mm). The skeleton of the fully soft actuator was cast from a silicone rubber (M4601, Elastosil) using 3D-printed molds.

For the skin materials, we used a 0.24 mm thick TPU sheet (American Polyfilm Inc.) for the soft linear actuator (Fig.2 (B) and Fig. S7(b)), the underwater hydraulic actuator (Fig.2 (D) and Fig. S7(d)), the electrics-embedded actuator (Fig. S7(e)), and the cylindrical lifter (Fig.3(B), Fig. S3(d), and Fig. S8(h)). A thinner TPU sheet (0.04 mm) was used for all the artificial muscles in the contraction, bending, and twisting demos (Fig.3), as well as for the cup-shaped gripper (Fig.3 and Fig. S8(h)). A 0.102 mm transparent PVC film (Vinyl) film was used to make the transparent actuator, and the miniature bio-compatible actuators (Fig.1 and Fig. S8(i)). A 0.025 mm PVA film was used as the skin for the water-soluble actuator (Fig.2(C) and Fig. S7(c)), and the 2.6 g light-weight actuator's skin is made of a 0.038 mm polyester sheet

(Fig.4(A). A 0.48 mm thick polyurethane-coated nylon fabric sheet (McMaster-Carr Supply Company) was used to make the actuator for the maximum-force production. A 0.34 mm thick TPU-coated nylon fabric sheet (Seattle Fabrics Inc.) was used to make the skins for the large lifter (Fig.1 and Fig. S8(j)) and most of the actuators used for static characterization. A 0.26 mm thick TPU-coated nylon fabric sheet from the same supplier was used to make the skins for actuators used for the large robotic arm in Fig. S7(f) and for the scalability test in Fig. S5(f).

The majority of the skins were directly sealed by an impulse heat sealer (AIE-410FL, American International Electric, Inc.) using proper sealing times for the different skin materials. For the miniature bio-compatible actuators shown in (Fig.1 (A) and Fig. S8(i)), double-coated medical tape (1552, 3M) was also used to adhere the skin materials together before applying heat sealing. This process ensures the sealing quality of the artificial muscles at small scales. The heat-sealing times for each muscle are listed in Table S1. In addition, we also give a list of materials for building FOAMs for different applications (Table S2).

4 Blocked-force measurement

The blocked forces were obtained using a universal testing machine (Instron 5544A, Instron Corporation). Each sample was preloaded with a 50N tension force in order to flatten the skin. To ensure a static test condition, the vacuum pressure was manually tuned through a vacuum regulator (Squire Cogswell) with a very slow rotational speed. We increased the pressure difference ΔP to -80 kPa (or -90 kPa), waited for 3 seconds, and then decreased it back to 0 kPa in each trial. This actuation-return trial was repeated five times on each actuator sample. A vacuum pressure sensor (MPXV4115VC6U, Freescale Semiconductor, Inc.) was used to detect the pressure inside of the actuation system. The generated force was recorded at 10 Hz from the Instron, and the signal from the vacuum sensor was recorded through a data acquisition device (BNC-2111, National Instruments).

5 Force-contraction experiment

To obtain the force-contraction relationship for each actuator, we applied a constant vacuum pressure to the actuator. The actuator was allowed to freely contract at a very low constant speed (1 mm/s) until the load decreased to 0 N. Then the Instron machine started to pull the actuator back to its original body length using the same speed in the contraction phase. This contraction-returning test was performed five times for each actuator, and both the contraction and force data were recorded at 10 Hz.

6 Measurement of skin deformation

To characterize skin deformation during actuating, we measured the depth of the geometrical vertex of the deformed skin within a skeleton void at different air pressure levels. As shown in Fig. S1(f), a laser displacement sensor (LK-031 laser head and LK-2001 controller, Keyence Corporation) was used to measure the displacement of the middle region of the local skin within a void. The sensor was vertically fixed on the Instron tester with a 25 mm reference distance to the actuator's skin surface. The flat skin surface before actuation (ΔP=0) was chosen as the reference plane for the displacement measurement. The laser beam was pointed perpendicularly to the skin's surface at the center of the void. Three linear zigzag actuators with different folds angles (30°, 60°, and 90°) were used for the skin deformation measurement. For each actuator, we performed the measurement for five loops (both the actuating and the releasing processes) using the same setting as used in the blocked-force experiments, and each actuator's displacement data was averaged over these five loops as shown in Fig. S1(g).

7 Cycle test and fatigue analysis

In the actuation cycle test, a linear zigzag actuator was vertically clamped to a metal stand, and a 1 kg load was attached to it. In each cycle, the actuator was powered for three seconds to lift up the attached load, then the vacuum supply was blocked and then air was filled into the actuator for another three seconds to release the contraction. This actuation-resting cycle was controlled using a miniature 12 V DC-powered solenoid valve (Parker Hannifin Corporation) with a micro-controller (Arduino Nano), and it was continuously repeated for 30,000 cycles over 50 hours.

The fatigue life of our artificial muscles significantly depend on the fatigue resistances of the skin materials and the skeleton materials. In general, the maximum stress/strain for both the skeleton and skin, along with the material type (e.g., brittle vs compliant materials and associated failure modes), need to be considered in designing an artificial muscle with a desired fatigue life.

For skeletons joined using flexure hinges or living hinges with a required fatigue life, the stress-life (S-N) and strain-life (ε-N) curves can be used either to find the best materials for a given hinge structure, or to find the stress/strain limit of a given material in order to optimize the structural design (*8, 9*).

For the compression spring based parallel skeletons, or the skeletons joined together by door hinges, the fatigue life can be very long since commercial hinges and springs are typically designed and fabricated to last several millions of cycles. However, the maximum load and other environmental conditions must be considered.

In addition, for artificial muscles with long fatigue lives, the skin should only experience elastic elongations under the expected loads. This requires that the maximum strains/stresses must not exceed the yield strains/strengths of the skin materials. Similarly, the S-N and ε-N

curves can be used either to choose the required materials, or to estimate the external load limits. If the S-N and ε-N characterizations are not available for chosen materials, then the hinge structure and the skin thickness need to be optimized to experience only elastic bending and elongation during actuation or external loading.

In this paper, we used a linear zig-zag muscle with a nylon skeleton for the cycling test. The strains and stresses of the skeleton's flexure hinges were estimated based on Euler-Bernoulli beam theory. The estimated maximum strain of the nylon hinge is approximately 13% at the center of the hinge, when it is fully closed. This value is far from the nylon filament material's strain levels at yield (27%) and at fracture (260%) according to the datasheet (*10*). For the skin material, the maximum stress was calculated to be approximately 4 MPa during actuation. We also characterized the nylon fabric sheet's ultimate tensile strength of approximately 100 MPa, and there was no yielding observed before material failure in our experiments. Our estimations indicate that both the nylon skeleton contractions and the nylon skin elongations are elastic deformations during cyclic actuation, thus a long fatigue life (>30,000 cycles) can be expected for this actuator.

8 Power density calculation

To estimate the actuator's power density, we performed dynamic load-lifting tests. A polyester-based light-weight actuator (mass: m_a = 2.6 g) was used in these tests. Vacuum (-80 kPa) was directly supplied to the actuator to quickly lift an object with mass m_{load}. In each test, the lifting process was recorded using a camera at 60 frames per second, and the lifting height h_{load} and time Δt were both obtained using an open source image analyzing software (Tracker, http://physlets.org/tracker/). The power density ρ was estimated using the following equation:

$$\rho = \frac{W_a}{m_a} = \frac{E_l/\Delta t}{m_a} = \frac{m_{load} \times g \times h_{load}}{m_a \Delta t} \tag{27}$$

where W_a represents the mechanical power of the load-lifting process, E_l is the final potential energy of the system, and g is the gravitational acceleration. The weight of the pressure source and associated plumbing are not included. This estimation was repeated five times for each lifting case, and the results were averaged (Fig. S6(e)).

9 Characterization of energy conversion efficiency

9.1 Mechanical energy efficiency of artificial muscle

To measure energy efficiency, we empirically measured the ratio between the input energy E_{in} and the work done by the system E_{out}. Water and air were both used as the internal fluids. In each trial, the fluid was slowly removed from the actuator using a syringe pump (Pump 11 Elite, Harvard Apparatus) at a constant low speed (ΔV_{air} = 80 mL/min, ΔV_{water} = 10 mL/min), while the pressure data was recorded. A vacuum sensor (MPXV4115V, Freescale Semiconductor) was used in the pneumatic tests, and a pressure transmitter (G2VAC, Ashcroft Inc.) was used in the hydraulic tests. The output energy was estimated by calculating the potential energy increase of the system. An object with known weight m_{load} was attached to the bottom of a vertically clamped actuator in each trial of the pneumatically-driven tests. To cancel water's weight, the actuator was placed horizontally on a desk (with a smooth glass surface), and a vertical load was tethered to its free-end by a Kevlar string over a smooth metal cylinder (plays as a pulley) in the hydraulically-driven tests. The load-lifting height h_{load} was measured using Tracker software. The energy efficiency can be written as followed:

$$\eta = \frac{E_{out}}{E_{in}} = \frac{m_{load} \times g \times h_{load}}{P\Delta V} = \frac{m_{load} \times g \times h_{load}}{\sum (P_t V_t)} \tag{28}$$

where g is the gravitational acceleration (9.81 m/s^2). P_t is the measured fluid pressure, and V_t is the volume change during each sampling step (0.1 s). This measurement was repeated five times for each lifting case, and the results were averaged as shown in Fig. S6(d).

9.2 System energy efficiency

In this experiment, the input energy was the electrical energy E_e used by the vacuum pump, and the output mechanical energy E_m was measured from a load lifting (m_{load} = 500 g) process driven by the linear muscle. The system's energy efficiency was calculated using Eq. **29** for the three DC-powered miniature pumps, and Eq. **30** for the AC-powered large pump.

$$\eta = \frac{E_{out}}{E_{in}} = \frac{E_m}{E_e} = \frac{m_{load} \times g \times h_{load}}{\sum (U_c \times I_t \times t_s)} \tag{29}$$

$$\eta = \frac{E_{out}}{E_{in}} = \frac{E_m}{E_e} = \frac{m_{load} \times g \times h_{load}}{P_e \times \Delta t} \tag{30}$$

where g is the gravitational acceleration, and t_s is the length of the sampling step (0.001 s). The load lifting process was recorded using a camera, and the final lifting height h_{load} was measured using Tracker software. For the DC-powered pumps, a constant voltage U_c was supplied using a DC power supply (1666, B&K Precision Corporation), and the current I_t was measured through a hall-effect current sensor (ACS712, SparkFun Electronics & Allegro MicroSystems). For the AC-powered pump, we calculated the input electrical energy using the pump's given power level P_e (approximately 380 W) and its working time Δt. In order to synchronize the experimental data, a reflective optical sensor (TCRT1000, Vishay Semiconductors) was placed under the load to detect the starting moment of the lifting process. The internal pressure was also measured during each test. The data from the current sensor, the vacuum pressure sensor, and the optical sensor were recorded through a data acquisition device (USB-6009, National Instruments). We conducted five measurements for each pump, and the systems' average energy efficiencies are shown in Fig. S6(c).

10 Bandwidth characterization of the light-weight muscle

To characterize the bandwidth of the artificial muscle system (including valves), we conducted a group of load lifting experiments (load: 500 g) using a light-weight linear zigzag muscle made of polyester (weight: 2.6 g, length: 10 cm). A micro-controller (Arduino Nano) was used to generate the control signal for a 12 V DC-powered solenoid valve (V^2, Parker Hannifin Corporation). A sinusoidal chirp voltage (amplitude: 5 V; frequency: from 0.1 to 3 Hz, increased 0.1 Hz after each cycle) was supplied to the valve in order to control the input vacuum pressure of the muscle. The muscle's load lifting motion was recorded by a camera and then analyzed using Tracker software. We compared the input voltage of the valve and the output contraction of the muscle, and generated a Bode diagram of this system as shown in Fig. S5(e).

11 Scalability of the artificial muscle

For small FOAMs at the millimeter or centimeter scales, many monolithic methods can be used for skeleton fabrication (*11*), including 3D-printing (*12*), self-folding (*13–15*), pop-up MEMS (*16, 17*), laser-cutting (*18–20*), soft lithography (*21, 22*), and photo-lithography (*23, 24*), etc. However, the fabricated structures must have sufficient space to accommodate the necessary fluidic components. Some processes, for example multi-layer soft lithography, can enable the simultaneous integration of microfluidic lines in the skeleton or skin, easing some assembly challenges. Below a certain scale (roughly micrometer scales), jamming and clogging would likely occur due to the small cross-section area. In addition, the skin material is another limitation for small-scale FOAMs, since the skin's thickness and bending stiffness might become non-negligible during the contraction.

To build muscles at the meter-scale or even beyond, monolithic fabrication processes would become very difficult. As an alternative to monolithic fabrication, large actuators would likely

require assembly by joining multiple discrete parts. Depending on the materials and dimensions, these separate parts can be fabricated using various methods, such as laser-cutting, 3D-printing, and traditional subtractive machining. These parts can then either be hinged together as an assembly (e.g., a group of rigid plates joined together by traditional hinges or flexure/living hinges). The materials used for large skeletons must be strong enough to prevent buckling under large compressive loads. In addition, the skin material's yield and tensile strengths must to be considered for building a large muscle with safe actuation and long fatigue life.

Furthermore, the skin sealing process will become challenging for both small-scale and large-scale fabrication. In our fabrication method, a muscle requires the skin to be sealed tightly, enclosing the skeleton and with no leaks. Thus the strategy for a reliable and easy sealing at both extremely small and large scales needs to be investigated in future work.

To investigate the scalability of our artificial muscles, we designed and fabricated a group of five actuators using a same linear zigzag pattern (60-degree folds) for the skeletons at different scales.

We built a 60-mm wide actuator as the standard size (ID: $\times 1$), then downsized to a $\frac{1}{2}\times$ (ID:$\times\frac{1}{2}$) and a $\frac{1}{3}\times$ width actuator (ID: $\times\frac{1}{3}$). In addition, two larger actuators were created at $\frac{3}{2}\times$ and $2\times$ wider than the standard actuator (ID:$\times\frac{3}{2}$ and$\times 2$). Therefore, the width ratio of the actuator is approximately $\frac{1}{3} : \frac{1}{2} : 1 : \frac{3}{2} : 2$, and the ratio of the cross-sectional area is $\frac{1}{9} : \frac{1}{4} : 1 : \frac{9}{4} : 4$, from the smallest to the largest one. The dimensions of the five actuators are shown in Fig.S5(f) and Table S1.

The skeleton of the $\times 2$ actuator consists of two 3D-printed ABS ends, and seven laser-cut acrylic plates. Those components are joined together by eight 3D-printed flexure hinges made of a nylon composite material (Onyx, Markforged). The other four smaller skeletons were directly 3D printed using the same nylon composite material. A 0.26-mm-thick nylon fabric sheet was used to make the skins for all the five actuators.

We conducted blocked force measurements for the five actuators and the results are shown in Fig.S5(g). In general, we can find that the larger the actuator, the lager the blocked force (for the same vacuum pressure). The largest actuator produced a blocked force of approximately 490 N, and the smallest actuator generated a blocked force of approximately 30 N, at -60 kPa pressure. We then normalized the blocked forces (at -20 kPa, -40 kPa, and -60 kPa, respectively) and the cross-sectional areas of all other four actuators compared to the standard actuator ($\times 1$). Fig.S5(h) reveals the relationship between these two normalized scales. The blocked forces of these actuators change proportionally with the cross-sectional areas. There was no significant deviation from this trend in the blocked force observed from our experiments. These results demonstrate the scalability of the FOAM concept, and follow intuition that greater forces can be produced using larger muscles.

12 Comparison with air cylinders and other elastomer-based artificial muscles

Inspired by the cold gas-pressure folding idea (*25*), we developed this fluidic artificial muscle architecture. Our artificial muscles have fundamental novelty and are different from traditional pneumatic cylinders/pistons and elastomer-based actuators(e.g., VAMPs) (*26*).

The principle of operation (physics) of our system is novel. For both pneumatic cylinders/pistons (Fig. S2(a)) and VAMPs (Fig. S2(b)), their forces are produced on the movable rigid surface that separates the high and low pressure volumes of the actuators, so the forces are limited by their cross-sectional areas. However our system primarily relies on the tension force generated on the actuator's wall surface plus a minor part of the force produced on its bottom surface (not a necessary component), thus the output force is not limited by the cross-sectional area (Fig. S2(c)). Therefore, our artificial muscles can generate significantly higher actuation stress (force) than other pneumatic actuators.

Our system's architecture is fundamentally novel. Air cylinder's contraction relies on the sliding motion of its piston head along the inner surface of its chammber. VAMPs generate contractions through the buckling of their elastomeric bodies (*26*). Our artificial muscles' contractions are achieved through the folding of origami-like skeletons.

Moreover, the fabrication method for most of the elastomeric actuators relies on casting complex geometries of elastomeric materials, limiting scalability (*27, 28*). However, our artificial muscles' fabrication is simply a skeleton-bagging process, thus it is much simpler and more scalable compared to other elastomeric actuators.

In addtion, our artificial muscles can use a wider variety of materials and geometries compared to others. Origami structures and fibers have previously been used as the constraining layers (*29, 30*) and embedded components (*31*) to provide reinforcement and programmability in pneumatic elastomeric actuators. However, these actuators are usually driven by compressed air at low pressures to produce limited forces and torques, due to the fragility of the stretched/inflated elastomeric materials.

Fig. S2(g) presents a summary of the comparison between our artificial muscles and the other two vacuum-driven actuators. To demonstrate the advantage of actuation force, we measured and compared the blocked force and free contraction of our linear zigzag muscles and a commercial air cylinder (Fig. S2(d-f)). The linear muscles are made of nylon materials, and the details of these muscles are shown in Fig. S2(h) and (i). The air cylinder (316-DXP-00MC, Bimba Manufacturing Company) is double-acting and made of stainless steel (bore size: 50.8 mm, stroke length: 152.4 mm). We applied a vacuum (0 to -90 kPa) to these actuators and recorded both the blocked forces and the internal pressures. The actuation stresses were calculated based on each actuator's cross-sectional area, and the comparison is shown in Fig. S2(f). One of the linear zigzag muscles (#4 in Fig. S2(i)) produced a contractile stress of approximately 640 kPa at -90 kPa vacuum pressure, and this is more than seven times greater than the

stress generated by the air cylinder at the same pressure level.

13 Comparison with other popular fluid-driven artificial muscles

To demonstrate the main advantages of the FOAM concept, we compared our technology with other popular fluidic artificial muscles. Although it is difficult to quantitatively compare these (often very different) artificial muscles, Table S3 lists all the accessible information/data among these related technologies. From the data and information in the table, the key advantages of FOAMs are very high force-to-weight ratio, large programmable contraction motion, low cost, wide material choice, and ease of fabrication.

14 Actuators driven by positive pressure

Our actuator can also be driven by a positive pressure difference. In this case the skin needs to be fixed on the skeleton. This fixation process can be achieved by gluing, bonding, tying, riveting, welding, etc. Once the internal pressure becomes higher than the external pressure, the skin will be driven to deform outwards by this pressure difference. The tension force produced on the skin will then actuate the skeleton structure to contract. As shown in Fig. S3(a) and Movie S4, a linear actuator rests in a flat strip structure. Its skin is adhered to the joints of a polyester-based unfolded zigzag skeleton. When this actuator is inflated with air using a syringe, the flat skeleton will be driven to fold to a zigzag structure while generating a contraction and a pulling force along its axial direction.

We should note that if a skin is fixed on a foldable skeleton, then the muscle can be driven by either a positive pressure or a negative pressure. As shown in Fig. S3(b), a polyester-based linear zigzag skeleton is covered by a thin polyester film. Each fold of the skeleton has an initial angle of approximately 120 degrees, and the skin is bonded at each fold's joint. This structure

allows the skin to expand outwards or contract inwards upon a positive pressure or a negative pressure; the skin tension force pulls the skeleton to fold in both cases. Therefore, this linear muscle can contract and lift a load using either a positive pressure or a negative-pressure.

We characterized the force-contraction relation on another linear actuator made by stronger materials. In this actuator, a nylon fabric skin is zip-tied on a 3D-printed nylon skeleton as shown in Fig. S3(c). This actuator can generate a contraction of approximately 10 mm and produce a pulling force of approximately 70 N at a very low pressure (30 kPa). This kind of actuator has a similar working principle as the one used in pouch motors (*32*) and Peano muscles (*33*), however using the transformable skeletons offers a greater programmability for our actuators.

15 Actuators driven by two different fluids

To demonstrate actuation when driven by two different fluids inside and outside of the skin, we set up a load-lifting experiment. In this hydraulically-driven actuator, a metal compression spring is used as the skeleton, and the skin is made of a transparent thermoplastic polyurethane (TPU) film (thickness: 0.24 mm), then blue-colored water is fully filled inside of the skin without air bubbles. In this demo, the actuator is vertically clamped to a metal stand, and a 1 kg load is attached to its end. A syringe pump is connected to the actuator through a transparent plastic tube. As shown in Fig. S3(d) and Movie S5, when the water is slowly removed from the actuator (ΔV = 80 mL/min), the attached weight is lifted and the actuator contracts. This demo shows that our artificial muscle can still work using water as the internal fluid and air as the external fluid.

16 Failure analysis of skeleton design

For the skeleton design and fabrication, the two common failures are wall buckling, and skeleton sliding. To characterize the performance of the actuator with a buckled skeleton, we fabricated two linear actuators with different wall thickness for comparison. Their skins are made of the same nylon fabric sheet (thickness: 0.34 mm), and the skeletons were 3D-printed using the same zigzag pattern (45 degree angle for each fold). However, one actuator's wall thickness is 3 mm, and the wall thickness of another actuator is only 1 mm as shown in Fig. S4(a). According to Euler's critical load formula for buckling, the 1-mm-thick skeleton has a lower critical compressive force than the 3 mm thick skeleton for the skeleton buckling. In our experiments, the actuator with the thinner skeleton buckled when the internal pressure was reduced lower than -40 kPa, whereas the actuator with the thicker skeleton performed normally without buckling (Fig. S4(a)). As can be seen in Fig. S4(d), once the actuator's skeleton buckled, its blocked force increased slower than the unbuckled actuator, as the internal pressure decreased from -40 kPa to -70 kPa. The buckled actuator produced a peak force of approximately 80 N at -70 kPa – 20% less than the force produced by the unbuckled actuator at the same pressure. The maximum hysteresis of the buckled actuator increased to 10 kPa, twice that of the unbuckled actuator. This reduced performance can be attributed to the dramatically changed structural geometry and the input energy lost to the elastic deformation of the buckled skeleton. From Fig. S4(g), we also observed a more than 50% decrease in the contraction of the buckled actuator compared to the unbuckled actuator at the same driving pressure (-70 kPa). This is mainly due to the incomplete folding contraction of the buckled skeleton. In order to prevent skeleton buckling, the critical load requirement needs to be considered in the skeleton's structural design and material selection.

To investigate the sliding effect on the skeleton, we compared two linear zigzag skeleton

performances. As shown in Fig. S4(b), these two zigzag-shaped skeletons are made of 3D-printed nylon. One actuator has nine identical voids (60-degree angle for each void), the other has two sizes of the voids (three 30-degree voids and six 60-degree voids). These unequal voids can cause unequal tension forces, and the contraction speeds will also differ for the unequal voids. The unequal force and contraction will induce sliding motions between the skin and skeleton (Fig. S4(b)). In our experiments, the sliding motion happened on the actuator with unequal size skeleton voids when the internal pressure decreased to around -10 kPa. As the results shown in Fig. S4(e), the blocked force increased more slowly compared to the actuator with identical skeleton voids. The blocked force approached approximately 85 N (at -70 kPa) – approximately 25% less than the actuator that did not exhibit sliding (115 N at -70 kPa). The maximum hysteresis of the sliding actuator was approximately 15 kPa, that is three times greater than the normal level of 5 kPa. In addition, the variation among five trials for the actuator that experienced sliding is much greater than the normal actuator. These performance reductions are due to the unexpected compression motion of the skeleton, as well as the energy loss caused by friction in the sliding motion. Similar as the buckled actuator, the contraction of the sliding actuator was also significantly reduced from 75 mm to 30 mm (Fig. S4(h)). This large reduction (approximately 60%) of the contraction is due to the incomplete compressive folding of the zigzag skeleton and the motion separation between the skin and the skeleton. There are two solutions for avoiding the undesired sliding motion: first, designing and fabricating the skeleton voids with identical sizes; second, fixing the skin to the skeleton to prevent sliding.

17 Effect of skin material

To explore the effect of the skin material, we created actuators with a TPU sheet (thickness: 0.24 mm, Young's modulus: 25 MPa) and a TPU-coated nylon fabric sheet (thickness: 0.34 mm, Young's modulus: 460 MPa). Both the actuators used 3D-printed nylon zigzag skeletons

(Fig. S4(c)). As we can see in Fig. S4(f), both the actuators showed approximately linear force-pressure relations. However, the TPU-skin actuator produced approximately 60% less force compared to the nylon-fabric-skin actuator at the same pressure difference. This reveals that the actuator with softer skin produces less force than the actuator with stiffer skin. This trend can also be observed from the comparison in Fig. S2(i). The primary reason for this force reduction is that the softer skin is elongated more than the stiffer skin at the same level of pressure difference. The skin length over each void becomes longer, and this reduces the radius of curvature at the contact points of each void. As predicted in our model using the parabolic approximation in Eqs. **4** and **6**, the generated tension force will be reduced at the contact points of each void as the skin length is increased. The maximum contractions of the two actuators both approached to approximately 60 mm as shown in Fig. S4(i). This is due to the same skeleton structures used in these two actuators, as the maximum contraction range is only determined by the skeleton's geometry if there is no buckling and sliding motion on the skeleton. In addition, we also found that the force contraction curve for the TPU-skin actuator is more linear than the nylon-fabric actuator. This indicates that using a softer skin can potentially offer a more linear contraction motion compared to using a stiffer skin, despite the reduction in force production.

18 Methods for skin-skeleton bonding

To enable secure bonding, we design a bonding plate on the bottom and top of each foldable structural void on the skeleton (Fig.S3(e)). Two hinges are used to join this bonding plate to the two walls of the void. This bonding plate is designed with a necessary minimum width to provide enough bonding surface for the skin. This design also brings a minimal change to the skeleton's geometry and structure, thus the skeleton's structural strength and programmability can be maintained.

As shown in Fig.S3(f), there are several methods for bonding the skin to the skeleton, and the particular strategy depends on the skin/skeleton materials, bonding strength, cost, and application.

Adhesive bonding can provide a quick, simple, and inexpensive approach for a low-profile bond over many materials. There are numerous adhesives for different materials combinations and various purposes, such as epoxy adhesives (high strength), acrylic adhesives (fast curing), urethane adhesives (high flexibility), etc.

Bonding the skin and skeleton via solvent bonding can offer high strength and good stress distribution over the bonded surface. Multiple types of solvents, such as acetone, ethanol, and methanol, etc., can be used for bonding. However, the compatibility of the solvent and the actuator materials needs to be investigated first (*34*).

Fusion welding is widely used for bonding thermoplastic materials due to its simplicity. It can also offer a relatively high bonding strength. Thermal-based welding (hot-plate, hot-air, infrared, and laser welding), friction-based welding (vibration, ultrasonic, and stir welding), and electromagnetic welding (induction, resistance, microwave, and dielectric welding) are the most widely used fusion bonding techniques (*35*). However, most of these methods are limited to bonding thermoplastic materials.

Another simple and efficient approach for skin-skeleton bonding is mechanical fastening, such as bolting, riveting, tying, and clamping, etc. The bonding strength of mechanical fastening can be very high, although the structure might become bulky and stress concentrations might become significant (Fig.S3(f)). In contrast to other bonding methods, mechanical fastening also allow us to replace or repair the skin or skeleton when failures happened.

19 Demonstration of control strategy for artificial muscles

19.1 Model-based open-loop control of actuation force

The output force of the artificial muscles can be controlled based on our simplified model. To demonstrate this model-based open-loop control, we conducted a force tracking experiment on a nylon-based linear zigzag actuator (90-degree folds). The desired output force F_{output} (N) was given as a sinusoidal wave (peak force: 140 N, frequency: 0.1 Hz), and the input pressure P_{input} (kPa) was calculated using a further simplified model as shown in Eq. **31**:

$$F_{output} \approx 2 \times P_{input} \tag{31}$$

The input pressure was then regulated by a vacuum pressure regulator (ITV0090-3MS, SMC Pneumatics). This pressure regulator was powered by a 24 V DC voltage from a power supply (1667, B&K Precision Corporation), and its control voltage (peak value: 7 V, frequency: 0.1 Hz) was supplied through an external function generator (DG2021A, RIGOL Technologies Inc.). The actual blocked force was measured at 10 Hz from the Instron machine, and the signal from the internal pressure was also recorded during the test. The comparison between the desired force and the actual force, as well as the measured internal pressure are shown in Fig. S5(d). In general, the output blocked force closely followed the input sinusoidal signal, indicating that our simplified mechanical model can be directly used for force control with a simple open-loop strategy at low frequencies. The maximum tracking error (approximately 35 N, 25% of the peak force) appeared during the unloading process, and this could be due to the unexpected sharp variations of the internal pressure. Therefore, we believe that the tracking error can be reduced by using a better pressure regulator in the pneumatic circuit.

19.2 Closed-loop control for the muscle contraction using sensor feedback

Sensors can be embedded into our artificial muscles to provide feedback information, and this information can be used to a closed-loop controller for the muscle. To demonstrate closed-loop control of muscle contraction, we built a nylon-based linear zigzag actuator (60-degree folds) with a reflective optical sensor (TCRT1000, Vishay Semiconductors) attached on its skeleton as shown in Fig. S5(a). This optical sensor reads the distance between the two plates of one fold, therefore it can be used as a contraction sensor for the linear muscle. The relation between the sensor's voltage reading and the muscle's actual contraction was characterized in the beginning by the experimental data. The muscle contraction was measured using video analysis (Tracker software), and the sensor's reading was recorded using a data acquisition device (USB-6009, National Instruments). The data and the fitted function (processed in MATLAB) are shown in Fig. S5(b). Based on this function, We then designed a simple proportional-integral (PI) controller for a contraction (position) tracking test, and the optical sensor's reading was used as the feedback signal.

To characterize the controller's performance, we conducted two groups of load lifting test with different load conditions. The muscle's contraction was recorded using a camera. The actuator's input pressure was controlled by a 12 V DC-powered solenoid valve (V^2, Parker Hannifin Corporation), and the pulse-width modulation (PWM) signal was generated from a micro-controller (Arduino Nano). The amplitude of this driven signal was calculated based on the desired contraction (position) and the optical sensor's voltage reading. In these tests, the muscle was commended to track contraction levels of 2 cm, 3 cm, and 4 cm for 5 seconds in each cycle. Fig. S5(c) shows the step responses of the desired contractions with different loads. These results indicate that the muscle can quickly and accurately respond to a desired contraction command using the PI controller (K_p=2.0, K_i=0.25). The system is also adaptive to different loads (500 g and 1 kg), and the maximum steady-state error of the contraction was

approximately 3 mm in our experiments.

20 Demonstration of a large robotic arm driven by FOAMs

To demonstrate the utility of FOAMs, we designed and built a large-scale modular robotic arm driven by nine FOAM actuators as shown in Fig. S7(f). This robotic arm consists of three identical segments, and each segment is supported by a bellows spring tube at the center with three linear muscles arranged around it. This tube also houses the pneumatic lines for the three muscles at each segment. Four round acrylic plates are used to separate all segments, and also to fix the bellows tubes and muscles. The skeleton of each muscle has a 60-degree linear zigzag pattern that was 3D-printed using TPU filaments. A 0.26-mm thick nylon fabric sheet was used as the skin for the muscle. Each of the fabricated muscle weighs approximately 24 grams, and it has a dimension of $16\times30\times130$ mm. A manifold of solenoid valves (V114-5FZ-X6, SMC pneumatics) and a micro controller (Arduino Mega) are used to control each of the nine muscles individually. In this demonstration, bending, rotation, contraction, and more complex motions can be achieved on this robotic arm through powering different combinations of these nine muscles.

Table S1 Details of the artificial muscles in this paper

ID	Skeleton		Skin			Dimension	Weight	Images	Function and performance
	Material	Geometry	Material	Thickness	Heat-sealing time	(mm)	(gram)		
#8	PEEK	linear zig-zag	PVC	0.102 mm	7 s	3.5×5×35	1	Fig.1 (a), Fig. S8(i)	miniature medical device
#9	PEEK	linear zig-zag	PVC	0.102 mm	7 s	5×13×70	1.6	Fig.1 (a), Fig. S8(i)	miniature medical device
#10	PEEK	linear zig-zag	PVC	0.102 mm	7 s	5×15×60	2	Fig.1 (a), Fig. S8(i)	miniature medical device
#11	nylon	linear zig-zag	nylon fabric	0.34 mm	16 s	100×150×750	748	Fig.1 (b), Fig. S8(j)	large lifter
#12	polyester	linear zig-zag	PVC	0.102 mm	7 s	20×140×160	20	Fig.2 (a), Fig. S7(a)	transparent muscle
#13	silicone rubber	linear zig-zag	TPU	0.24 mm	8 s	25×40×230	70	Fig.2 (b), Fig. S7(b)	soft muscle
#14	PVA	linear zig-zag	PVA	0.025 mm	6 s	30×40×200	10	Fig.2 (c), Fig. S7(c)	water-soluble muscle
#15	stainless steel	linear zig-zag	TPU	0.24 mm	8 s	15×60×160	18	Fig.2 (d), Fig. S7(d)	under-water muscle
#16	polyester	linear zig-zag	TPU	0.04 mm	4 s	15×40×190	3.5	Fig.3 (a), Fig. S8(a)	1D contraction muscle
#17	polyester	Miura-ori	TPU	0.04 mm	4 s	15×100×110	5.7	Fig.3 (b), Fig. S8(b)	2D contraction muscle
#18	polyester	magic ball	TPU	0.04 mm	4 s	70 (diameter)	8	Fig.3 (c), Fig. S8(c)	3D contraction muscle
#19	nylon	asymmetrical beam	TPU	0.04 mm	4 s	25×30×170	33	Fig.3 (d), Fig. S8(d)	bending muscle
#20	polyester	flasher pattern	TPU	0.04 mm	4 s	15×160×160	11	Fig.3 (e), Fig. S8(e)	contraction and rotation muscle
#21	polyester	Miura-ori	TPU	0.04 mm	4 s	15×100×110	5.7	Fig.3 (f), Fig. S8(f)	contraction and torsion muscle
#22	nylon	hinged beams	TPU	0.06 mm	5 s	30×100×160	55	Fig.3 (g), Fig. S8(g)	three-finger hand
#23	stainless steel	helical spring	TPU	0.24 mm	8 s	25 (diameter); 200 (length)	17	Fig.3 (h), Fig. S3(d), Fig. S8(h)	lifting and twisting muscle
#24	polyester	magic ball	TPU	0.04 mm	4 s	90 (diameter); 60 (height)	8	Fig.3 (h), Fig. S8(h)	cup-shaped gripper
#25	acrylic	linear zig-zag	TPU	0.24 mm	8 s	120×120×600	768	Fig. S7(e)	electronics embedded muscle
#26	polyester	linear zig-zag	TPU	0.04 mm	4 s	5×50×250	6	Fig. S3(a)	positive-pressure driven muscle
#27	polyester	linear zig-zag	polyester	0.038 mm	6 s	10×60×260	5.5	Fig. S3(b)	positive/negative-pressure driven muscle
#28	nylon	hinged beam	nylon fabric	0.34 mm	16 s	15×70×350	63	Fig. S3(c)	positive-pressure driven muscle
#29	polyester	linear zig-zag	polyester	0.038 mm	16 s	12×30×100	2.6	Fig.4	light-weight muscle
#30	nylon	linear zig-zag	TPU	0.24 mm	16 s	15×70×190	59	Fig. S4(c)	TPU-skin linear muscle
#31	nylon	linear zig-zag	nylon fabric	0.34 mm	16 s	15×70×190	58	Fig. S4(c)	nylon-skin linear muscle
#32	nylon	linear zig-zag	nylon fabric	0.34 mm	16 s	30×50×200	29	Fig. S4(a), (b)	normal-contraction muscle
#33	nylon	linear zig-zag	nylon fabric	0.34 mm	16 s	30×50×200	20	Fig. S4(a)	skeleton-buckling muscle
#34	nylon	unequal folds zig-zag	nylon fabric	0.34 mm	16 s	30×50×200	32	Fig. S4(b)	skeleton-sliding muscle
#35	nylon	linear zig-zag	nylon fabric	0.34 mm	16 s	30×50×220	36	Fig. S5(a)	muscle for position/force control
#36	Onyx	linear zig-zag	nylon fabric	0.26 mm	14 s	7.3×20×60	5.6	Fig. S5(f)	$\times\frac{1}{3}$ muscle for scalability test
#37	Onyx	linear zig-zag	nylon fabric	0.26 mm	14 s	11×30×90	16	Fig. S5(f)	$\times\frac{1}{2}$ muscle for scalability test
#38	Onyx	linear zig-zag	nylon fabric	0.26 mm	14 s	22×60×180	65	Fig. S5(f)	$\times 1$ muscle for scalability test
#39	Onyx	linear zig-zag	nylon fabric	0.26 mm	14 s	33×90×270	176	Fig. S5(f)	$\times\frac{3}{2}$ muscle for scalability test
#40	Onyx, acrylic, and ABS	linear zig-zag	nylon fabric	0.26 mm	14 s	44×120×360	510	Fig. S5(f)	$\times 2$ muscle for scalability test
#41	TPU	linear zig-zag	nylon fabric	0.26 mm	14 s	16×30×130	24	Fig. S7(f)	linear muscle for the large arm

Table S2 Recommendations for material combinations for different applications

Application scenario	**Skeleton material**	**Skin material**	**Fluid**
High/low temperature applications	PTFE or PAI	Kapton or PTFE films	Air or mineral oil
Medical applications	PEEK or PVC	PVC films	Air or saline
Light-weight/wearable applications	Foam or rubber	TPU-coated nylon fabrics	Air
Heavy-duty applications	Reinforced composites or metals	TPU-coated Kevlar fabrics	Air or water
Chemical-resistant applications	PVDF or PTFE	PVDF or PTFE films	Air or water
Disposable applications	PVA	PVA films	Air
Optical-transparency applications	Transparent acrylic or Polycarbonate	Transparent polyester or PVC films	Air or water
Moist environment applications	PET or stainless steel	Rubber or PET films	Air
Aircraft applications	PTFE or high-strength composites	Kapton or Mylar films	Air
Underwater applications	Stainless steel or composite epoxy materials	Rubbers or TPU-coated fabrics	Water

Table S3 Comparison of different fluid-driven artificial muscles

		FOAMs	**McKibben muscles (*36–38*)**	**VAMPs (*26, 39*)**	**Peano muscles/Pouch motors (*32, 33, 40*)**	**Pleated PAM (*41, 42*)**
Summary of fabrication	**Primary components needed** (excluding fluidic tubes and connectors)	Skeleton and skin materials.	Inner bladder, braided mesh sleeve, and clamps/ties.	Elastomer, molds, and glue.	Thermoplastic/composite sheet, stamps/clamps, and protection sheet/core material.	Pleated membrane, end closures, toothed parts, and epoxy resin.
	Main steps and processes	(1) Preparing the skeleton; (2) Preparing the skin; (3) Sealing the skin.	(1) Preparing the bladder; (2) Preparing the sleeve; (3) Inserting the bladder and clamping it with the sleeve.	(1) Preparing the molds; (2) Casting the elastomer; (3) Curing the parts; (4) Bonding the parts together.	(1) Preparing the sheets; (2) Preparing the stamps /clamps; (3) Sealing/laminating; (4) Removing the protection/core materials.	(1) Preparing the membrane; (2) Preparing the end closures; (3) Bonding the membrane to the toothed parts; (4) Fixing the ends.
	Minimum fabrication time (for building a single muscle)	$<$10 mins	10 to 30 mins	4 to 6 hours	Unknown	$\approx$ 2 hours
Material cost estimate		$<$\$1 (for a 10-cm long zigzag muscle made of polyester)	$<$\$10 (for a 1-ft long home-made McKibben muscle)	$<$\$2 (for a 4.6-cm long muscle made of Elastosil)	Unknown	Unknown
Programmability (output motion by a single muscle driven by a single fluidic input)		1D contraction 2D contraction 3D contraction Bending Rotation Twisting Multi-DoF motion with different rates	1D contraction	1D contraction 2D contraction Rotation	1D contraction Bending Rotation	1D contraction
Material choices for primary components		(a) Flexible materials: fabrics, elastomers, flexible plastics and composites, foams, etc. (b) Rigid materials: metals, rigid plastics and composites, etc.	Flexible materials: silicone/latex rubber and plastic/composite mesh.	Flexible materials: elastomers and 3D printed soft materials.	Flexible materials: thermoplastic sheets and textile-elastomer composite sheets.	Flexible materials: Kevlar fabric and polyester fabric (Kevlar reinforced).
Maximum contraction ratio		$>$90%	30%	45%	28%	40%
Maximum actuation stress (driven pressure)		640 kPa (at -90kPa)	$>$1,000 kPa (at 400kPa)	65 kPa (at -90kPa)	110 kPa (at 200kPa)	680 kPa (at 400kPa)
Maximum force-to-weight ratio		$>$10 kN/kg	8 kN/kg	$>$2.8 kN/kg	Unknown	$>$50 kN/kg
Low-profile actuation (no significant increase of cross-section/volume during actuation)		Yes (at negative pressure)	No	Yes	No	No
Operation pressure		Negative and positive	Positive (threshold $>$100 kPa)	Negative	Positive (threshold $<$10 kPa)	Positive (threshold $<$10 kPa)
Advantages		Safe, low-cost, programmable, large-contraction, and wide material choices.	Simple, powerful, and low-cost.	Safe, compliant, durable, large-contraction, and low-profile.	Simple, compact, low-cost, low threshold-pressure, and wide material choice.	Powerful, large-contraction, and low threshold-pressure.
Limitations		Possible sliding, buckling, and failures of the skeleton.	Small contraction ratio, high-threshold pressure, and bulky structure after contraction.	Low actuation-stress and long fabrication-time.	Low actuation-stress and small contraction ratio.	Bulky structure after contraction and long fabrication-time.

References

1. Michelena NF, Agogino AM (1988) Multiobjective hydraulic cylinder design. *Journal of Mechanisms, Transmissions, and Automation in Design* 110(1):81–87.

2. Madden JD, et al. (2004) Artificial muscle technology: physical principles and naval prospects. *IEEE Journal of Oceanic Engineering* 29(3):706–728.

3. Hunter IW, Lafontaine S (1992) A comparison of muscle with artificial actuators in *Solid-State Sensor and Actuator Workshop, 1992. 5th Technical Digest., IEEE*. (IEEE), pp. 178–185.

4. Full RJ, Meijer K (2001) Metrics of natural muscle function. *Electro Active Polymers (EAP) as Artificial Muscles, Reality, Potential, and Challenges* pp. 67–83.

5. Wehner M, et al. (2014) Pneumatic energy sources for autonomous and wearable soft robotics. *Soft Robotics* 1(4):263–274.

6. Ding Y, et al. (2014) Multi-joint actuation platform for lower extremity soft exosuits in *Robotics and Automation (ICRA), 2014 IEEE International Conference on*. (IEEE), pp. 1327–1334.

7. Davis S, Tsagarakis N, Canderle J, Caldwell DG (2003) Enhanced modelling and performance in braided pneumatic muscle actuators. *The International Journal of Robotics Research* 22(3-4):213–227.

8. Socie DF (1977) Fatigue-life prediction using local stress-strain concepts. *Experimental Mechanics* 17(2):50–56.

9. Riddell M, Koo G, O'Toole J (1966) Fatigue mechanisms of thermoplastics. *Polymer Engineering & Science* 6(4):363–368.

10. Markforged (2016) Mechanical properties of nylon (https://markforged.com/landing/material-data-sheet/). Online; accessed: 2017-09-30.

11. Zhang Y, et al. (2017) Printing, folding and assembly methods for forming 3d mesostructures in advanced materials. *Nature Reviews Materials* 2:17019.

12. Ahn BY, et al. (2010) Printed origami structures. *Advanced Materials* 22(20):2251–2254.

13. Tolley MT, et al. (2014) Self-folding origami: shape memory composites activated by uniform heating. *Smart Materials and Structures* 23(9):094006.

14. Liu Y, Boyles JK, Genzer J, Dickey MD (2012) Self-folding of polymer sheets using local light absorption. *Soft Matter* 8(6):1764–1769.

15. Ionov L (2013) 3d microfabrication using stimuli-responsive self-folding polymer films. *Polymer Reviews* 53(1):92–107.

16. Sreetharan PS, Whitney JP, Strauss MD, Wood RJ (2012) Monolithic fabrication of millimeter-scale machines. *Journal of Micromechanics and Microengineering* 22(5):055027.

17. Whitney JP, Sreetharan PS, Ma KY, Wood RJ (2011) Pop-up book mems. *Journal of Micromechanics and Microengineering* 21(11):115021.

18. Onal CD, Wood RJ, Rus D (2013) An origami-inspired approach to worm robots. *IEEE/ASME Transactions on Mechatronics* 18(2):430–438.

19. Rafsanjani A, Bertoldi K (2017) Buckling-induced kirigami. *Physical Review Letters* 118(8):084301.

20. Tang Y, et al. (2015) Design of hierarchically cut hinges for highly stretchable and reconfigurable metamaterials with enhanced strength. *Advanced Materials* 27(44):7181–7190.

21. Jackman RJ, et al. (1999) Three-dimensional metallic microstructures fabricated by soft lithography and microelectrodeposition. *Langmuir* 15(3):826–836.

22. Xu B, et al. (1999) Making negative poissons ratio microstructures by soft lithography. *Advanced Materials* 11(14):1186.

23. Brittain ST, Schueller OJ, Wu H, Whitesides S, Whitesides GM (2001) Microorigami: Fabrication of small, three-dimensional, metallic structures. *The Journal of Physical Chemistry B* 105(2):347–350.

24. Yan Z, et al. (2016) Controlled mechanical buckling for origami-inspired construction of 3d microstructures in advanced materials. *Advanced Functional Materials* 26(16):2629–2639.

25. Schenk M, Guest SD (2013) Geometry of miura-folded metamaterials. *Proceedings of the National Academy of Sciences* 110(9):3276–3281.

26. Yang D, et al. (2016) Buckling pneumatic linear actuators inspired by muscle. *Advanced Materials Technologies* 1(3):1600055.

27. Rus D, Tolley MT (2015) Design, fabrication and control of soft robots. *Nature* 521(7553):467–475.

28. Shepherd RF, et al. (2011) Multigait soft robot. *Proceedings of the National Academy of Sciences* 108(51):20400–20403.

29. Paez L, Agarwal G, Paik J (2016) Design and analysis of a soft pneumatic actuator with origami shell reinforcement. *Soft Robotics* 3(3):109–119.

30. Connolly F, Walsh CJ, Bertoldi K (2017) Automatic design of fiber-reinforced soft actuators for trajectory matching. *Proceedings of the National Academy of Sciences* 114(1):51–56.

31. Martinez RV, Fish CR, Chen X, Whitesides GM (2012) Elastomeric origami: programmable paper-elastomer composites as pneumatic actuators. *Advanced Functional Materials* 22(7):1376–1384.

32. Niiyama R, et al. (2015) Pouch motors: Printable soft actuators integrated with computational design. *Soft Robotics* 2(2):59–70.

33. Sanan S, Lynn PS, Griffith ST (2014) Pneumatic torsional actuators for inflatable robots. *Journal of Mechanisms and Robotics* 6(3):031003.

34. Tsao CW, DeVoe DL (2009) Bonding of thermoplastic polymer microfluidics. *Microfluidics and Nanofluidics* 6(1):1–16.

35. Yousefpour A, Hojjati M, Immarigeon JP (2004) Fusion bonding/welding of thermoplastic composites. *Journal of Thermoplastic Composite Materials* 17(4):303–341.

36. Chou CP, Hannaford B (1996) Measurement and modeling of mckibben pneumatic artificial muscles. *IEEE Transactions on Robotics and Automation* 12(1):90–102.

37. (2014) Pneumatic artificial muscles (https://softroboticstoolkit.com/book/pneumatic-artificial-muscles). Online; accessed: 2017-09-30.

38. (2008) Build air muscles (http://forums.trossenrobotics.com/tutorials/how-to-diy-128/build-air-muscles-2212/). Online; accessed: 2017-09-30.

39. Yang D, et al. (2015) Buckling of elastomeric beams enables actuation of soft machines. *Advanced Materials* 27(41):6323–6327.

40. Veale AJ, Xie SQ, Anderson IA (2016) Characterizing the peano fluidic muscle and the effects of its geometry properties on its behavior. *Smart Materials and Structures* 25(6):065013.

41. Villegas D, Van Damme M, Vanderborght B, Beyl P, Lefeber D (2012) Third–generation pleated pneumatic artificial muscles for robotic applications: Development and comparison with mckibben muscle. *Advanced Robotics* 26(11-12):1205–1227.

42. Daerden F, Lefeber D (2002) Pneumatic artificial muscles: actuators for robotics and automation. *European Journal of Mechanical and Environmental Engineering* 47(1):11–21.

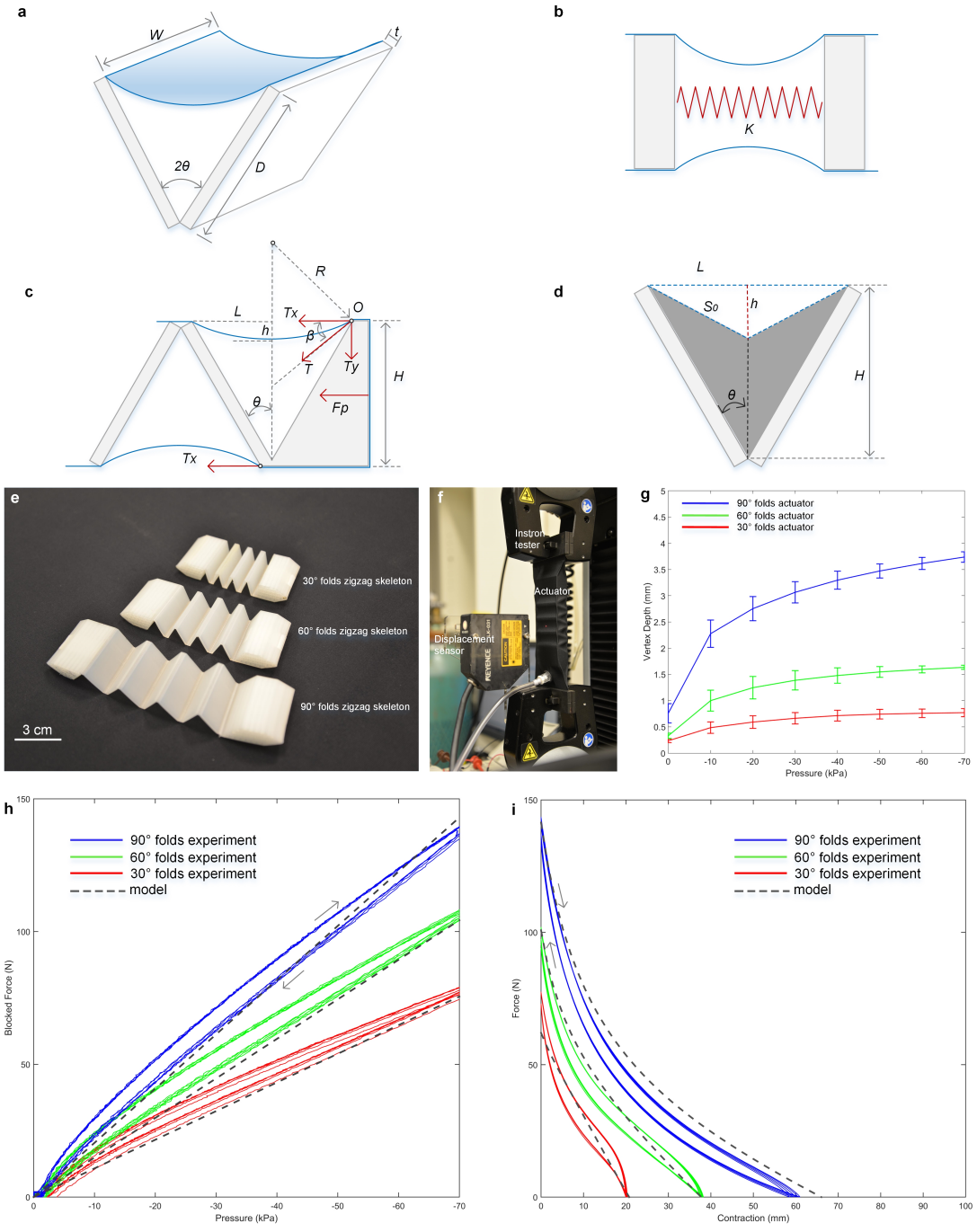

Fig.S 1. Mechanical modeling and validation. **a**, Hinged plates model. **b**, Parallel plates model. **c**, Force balancing model for the blocked-force estimation. **d**, Triangle-approximation for the fluid work estimation. **e**, 3D-printed nylon skeletons for model validation. **f**, Laser measurement of skin deformation. **g**, Measured skin deformation. The mean is plotted along with error bars representing the standard deviation from five trials. **h**, Blocked-force comparison between the model estimation and experimental data. **i**, Force-contraction comparison between the model estimation and experimental data.

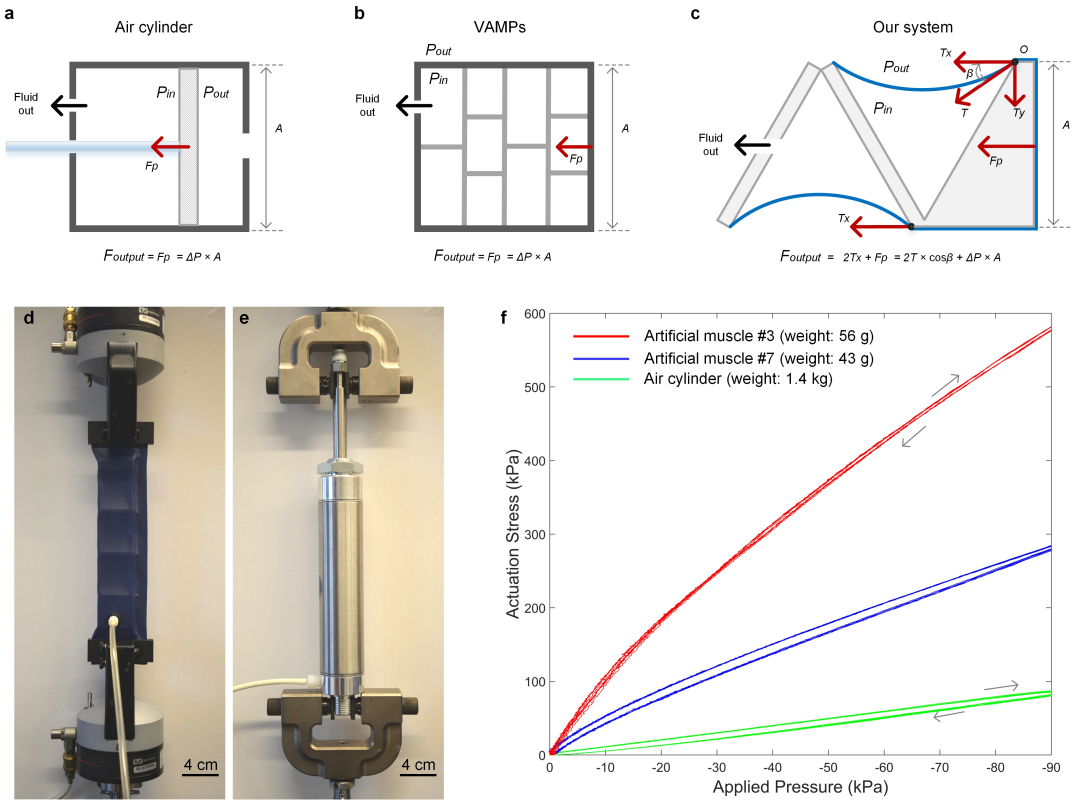

g

Actuator	Weight (gram)	Maximum actuation stress (at -90 kPa vacuum)	Maximum contraction (at -90 kPa vacuum)	Structural movement
Air cylinder	≈ 1,400	85 kPa	50%	Sliding
VAMPs	≈ 24	65 kPa	45%	Buckling
Our muscle #3	56	582 kPa	31%	Folding
Our muscle #7	43	285 kPa	50%	Folding

h

Skin material	Thinckness	Young's modulus
Thermoplastic polyurethane (TPU)	0.24 mm	≈ 25 Mpa (10% strain)
TPU-coated nylon fabric #1	0.34 mm	≈ 460 Mpa
TPU-coated nylon fabric #2	0.48 mm	≈ 1000 Mpa

i

ID	Skeleton geometry	Muscle dimension (mm, without ~ 50 mm handle)	Skin thickness (mm, nylon fabric)	Muscle weight (gram)	Maximum force/stress (at -90 kPa vacuum)	Maximum contraction (at -90 kPa vacuum)
#1	30° zigzag	50 × 46 × 16	0.48	41	237 N / 322 kPa	9 mm / 18%
#2	60° zigzag	80 × 46 × 16	0.48	48	324 N / 440 kPa	22 mm / 28%
#3	90° zigzag	150 × 46 × 16	0.48	56	428 N / 582 kPa	46 mm / 31%
#4	120° zigzag	170 × 41 × 15.5	0.48	55	407 N / 640 kPa	12 mm / 7%
#5	30° zigzag	50 × 45.5 × 15.5	0.34	33	95 N / 135 kPa	19 mm / 38%
#6	60° zigzag	80 × 45.5 × 15.5	0.34	37	145 N / 206 kPa	36 mm / 45%
#7	90° zigzag	130 × 45.5 × 15.5	0.34	43	201 N / 285 kPa	65 mm / 50%

Fig.S 2. Comparison with air cylinders and other elastomer-based artificial muscles. **a**, **b**, **c**, Comparison on the principle of operation, **(a)** air cylinder, **(b)** VAMPs, and **(c)** our artificial muscle (linear zigzag skeleton). **d**, **e**, Blocked force measurement, **(d)** nylon-based zigzag muscle (#4), and **(e)** commercial air cylinder. **f**, Comparison of the actuation stress of the air cylinder and our artificial muscles. **g**, Comparison of negative-pressure-driven fluidic actuators. **h**, Comparison of the skin materials. **i**, Comparison of the nylon-based linear zigzag muscles.

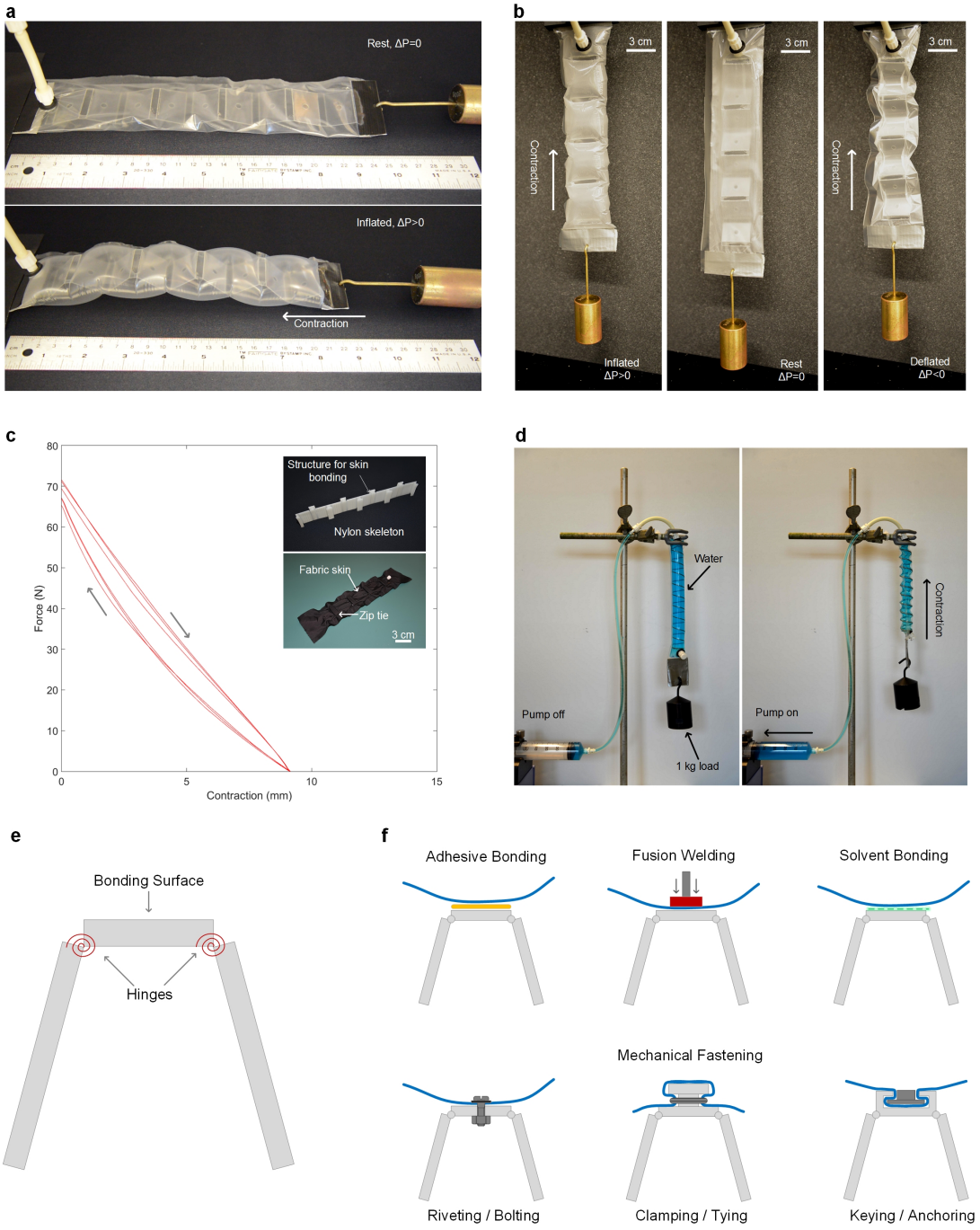

Fig.S 3. Artificial muscles driven by positive pressure and different fluids. **a**, A demo of positive-pressure-driven contraction. **b**, A linear zigzag muscle that can be powered to contract by either a positive-pressure or a negative-pressure. **c**, Force-contraction experiment on a positive-pressure-driven actuator. **d**, Water-driven load lifting test using a spring-based muscle. **e**, A hinge structure for skin-bonding. **f**, Different methods for skin-skeleton bonding.

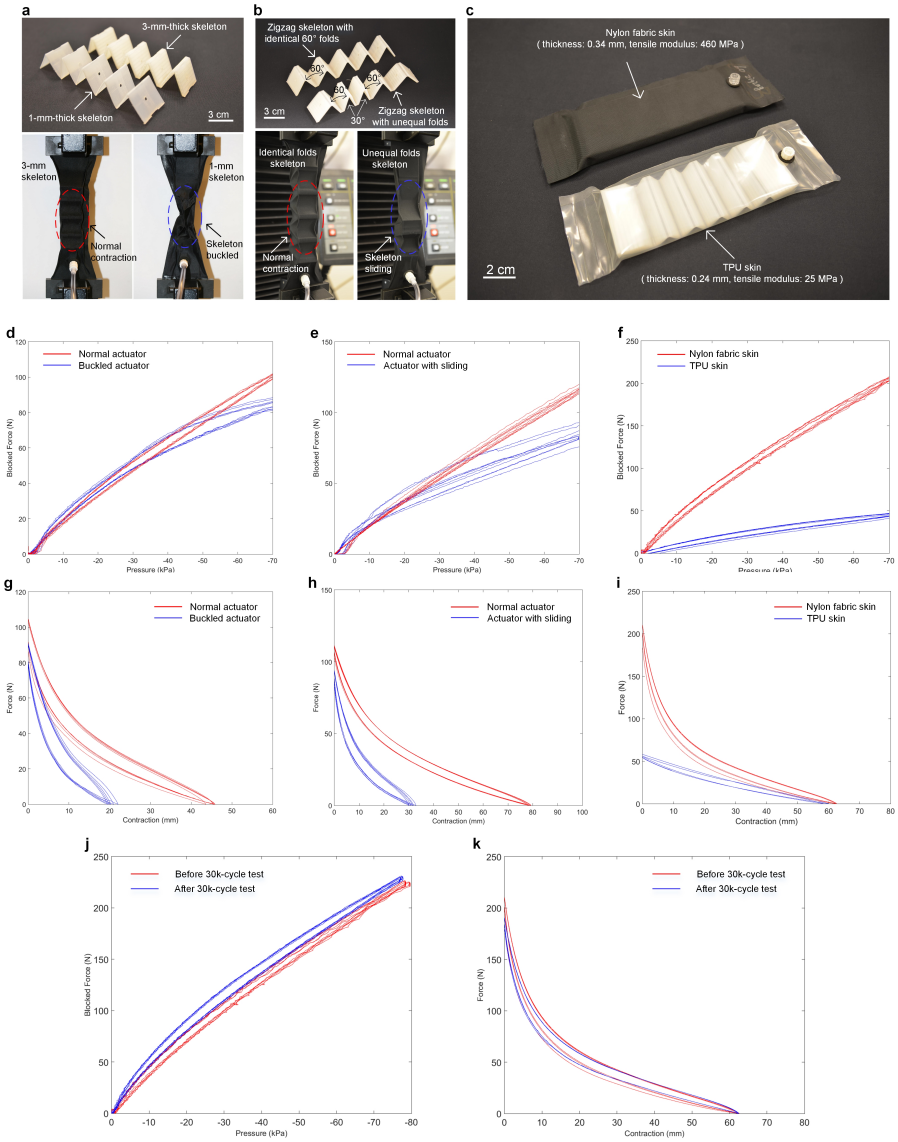

Fig.S 4. Failure analysis of skeleton design, effect of skin material, and cycle test. **a**, Two skeletons with different wall thicknesses. The thick-wall skeleton contracted normally, but the thin-wall skeleton buckled. **b**, Two skeletons with different geometries. The skeleton with identical folds contracted normally, however the skeleton with unequal folds exhibited sliding. **c**, Two similar actuators using different skin materials. **d**, **g**, Experimental comparison on the actuators using two skeletons with different thicknesses, **(d)** blocked-force and **(g)** force-contraction relation (ΔP = -70 kPa). **e**, **h**, Experimental comparison on the actuators using identical-folds skeleton and unequal-folds skeleton, **(e)** blocked-force and **(h)** force-contraction relationship (ΔP = -70 kPa). **f**, **i**, Experimental comparison on the actuators using nylon-skin and TPU-skin, **(f)** blocked-force and **(i)** force-contraction relationship (ΔP = -70 kPa). **j**, **k**, Experimental comparison on the actuator before and after 30,000-cycle runs, **(j)** blocked-force and **(k)** force-contraction relationship (ΔP = -70 kPa).

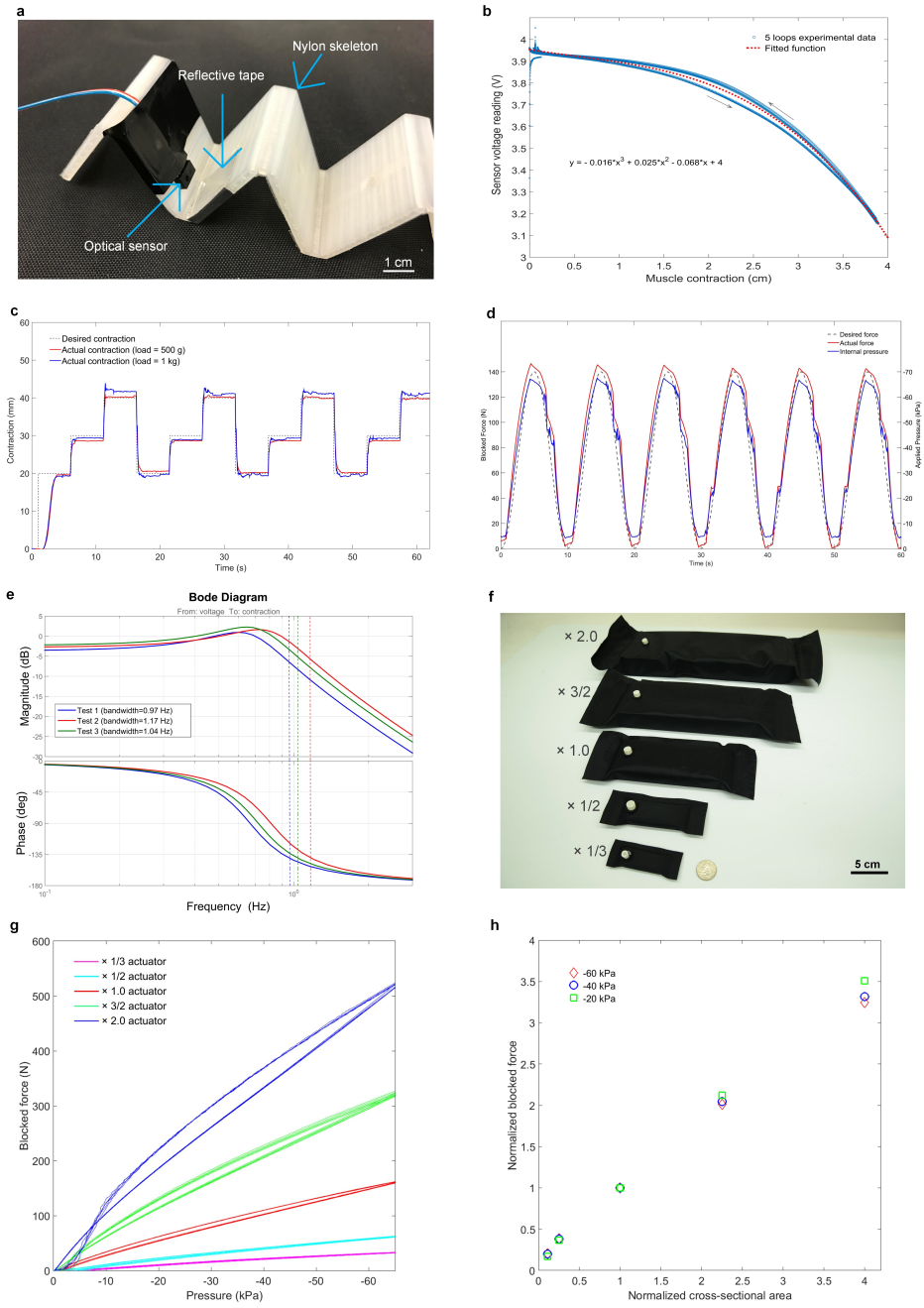

Fig.S 5. Demonstrations of control strategy, bandwidth characterization, and scalability. **a**, A zigzag skeleton with an optical contraction sensor. **b**, Empirical characterization of the optical contraction sensor. **c**, Step responses of the muscle contraction using a closed-loop PI controller. **d**, Open-loop force tracking result at 0.1 Hz. **e**, Bandwidth characterization of the 2.6-gram zigzag muscle with a solenoid valve (load = 500 g). **f**, Five linear zigzag muscles at different scales. **g**, Blocked forces of the these five muscles. **h**. Normalized relationship between the muscles' cross-sectional areas and blocked forces.

a

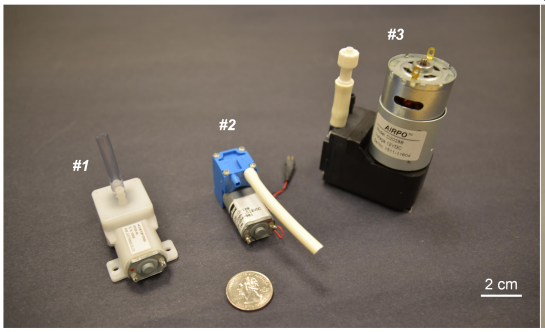

b

c

ID	Brand	Model	Type	Weight (gram)	Voltage	Maximum flow rate (LPM)	Maximum vacuum pressure (kPa)	Muscle system energy efficiency (electrical energy to mechanical energy)
#1	KOGE	KPV20A-6A	diaphragm	45	6 V DC	2.5	≈ -35	4.57 %
#2	Parker	CTS	diaphragm	46	12 V DC	2.5	≈ -67	3.76 %
#3	AIRPO	D2028B	diaphragm	288	12 V DC	15	≈ -65	2.51 %
#4	VIOT	VPD5	rotary vane	11,200	110 V AC	156	≈ -96	0.31 %

d

Mechanical energy conversion efficiency

Load	Air-driven	Water-driven
0.2 kg	13.08 %	44.58 %
0.5 kg	20.26 %	59.48 %
1.0 kg	22.73 %	51.72 %

e

Power density

Load	Average power density	Peak power density
1 kg	1.04 kW/kg	1.85 kW/kg
2 kg	1.32 kW/kg	2.08 kW/kg
3 kg	1.19 kW/kg	1.80 kW/kg

Fig.S 6. Characterizations of energy efficiency and power density. **a**, DC-powered miniature pumps (diaphragm) used in the tests. **b**, AC-powered large pump (rotary vane) used in the tests. **c**, Comparison of the vacuum pumps. **d**, Efficiency of mechanical energy conversion of the actuator. **e**, Power density of the actuator.

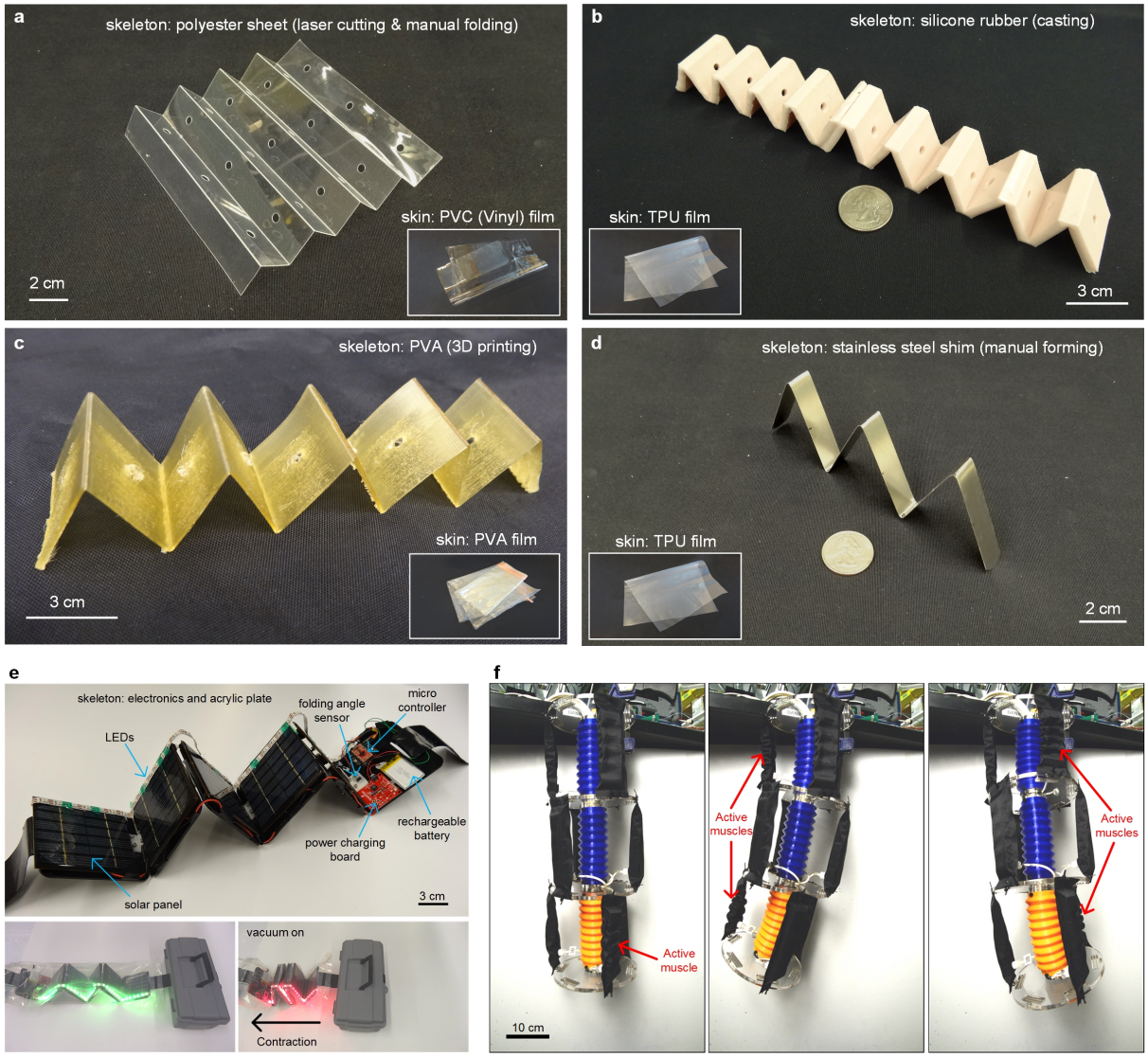

Fig.S 7. a, Materials for the transparent actuator. **b**, Materials for the soft actuator. **c**, Materials for the water-soluble actuator. **d**, Materials for the under-water actuator. **e**, An actuator with electronics embedded. **f**, A large robotic arm driven by nine zigzag artificial muscles.

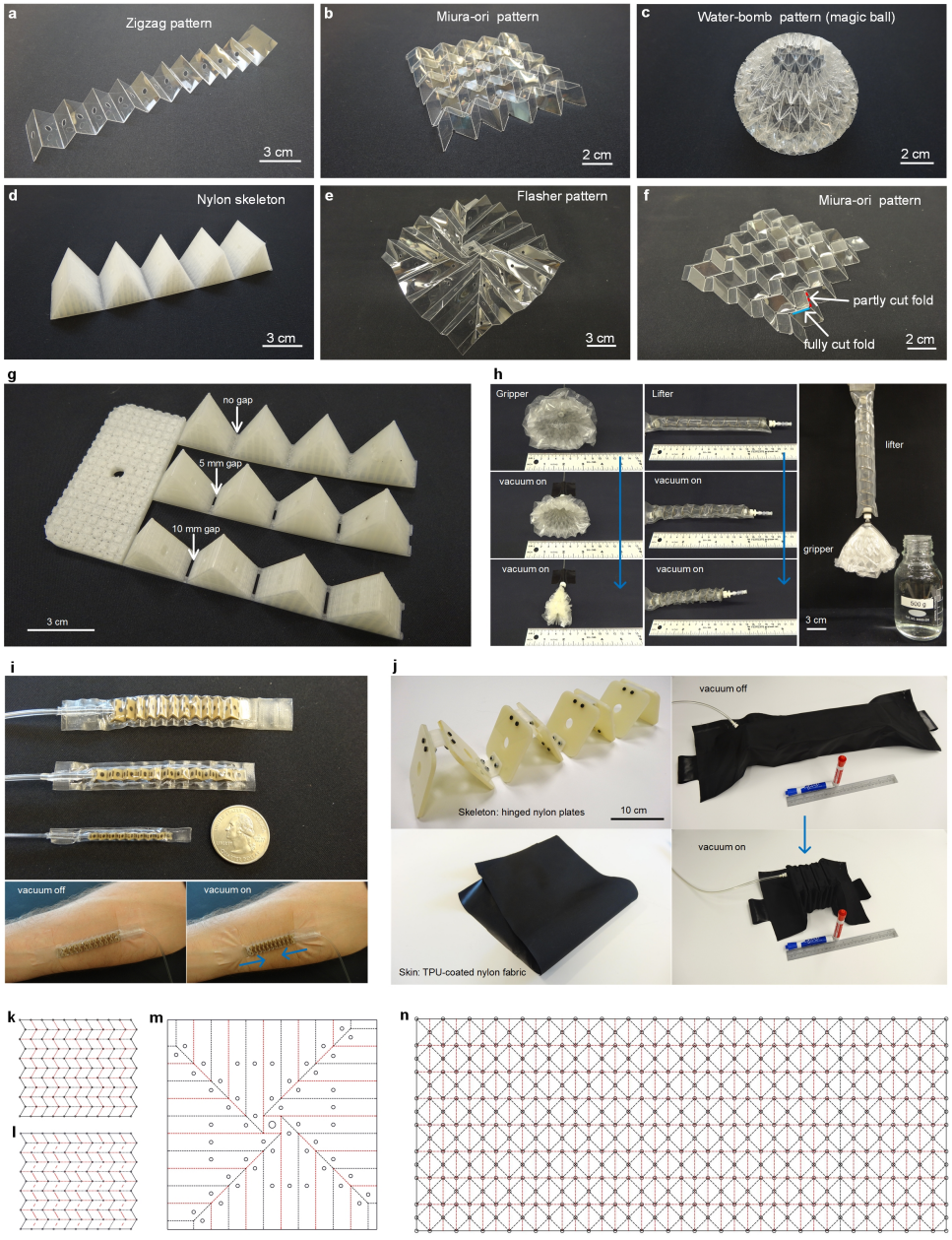

Fig.S 8. Skeleton geometries for the various actuation motions shown in this paper. **a**, 1D contraction. **b**, 2D contraction. **c**, 3D contraction. **d**, The bending motion. **e**, The combined contraction and rotation. **f**, The combined contraction and torsion. **g**, The skeleton for the three-finger robotic hand. **h**, The gripper and the lifter components for the robotic arm. **h**, Millimeter-scale linear zigzag actuators made from bio-compatible materials, and these actuators can be used for medical applications, such as skin tensioning or for wearable assistive devices. **i**, The large lifter uses hinged nylon plates as its skeleton. **k-n**, The crease patterns for the origami skeletons in (b), (f), (e), and (c), respectively. The red dashed lines represent mountains and the black dashed lines are valleys. The circles are included to reduce stress concentrations and to enhance fluid circulation.